Progress In Electromagnetics Research, Vol. 142, 721–742, 2013

PERFORMANCE ANALYSIS OF BISTATIC INTERFEROMETER BASED ON SPACEBORNE SAR

Qilei Zhang* **and Wenge Chang**

College of Electronic Science and Engineering, National University of Defense Technology, Changsha, Hunan 410073, P. R. China

Abstract—This paper presents the performance analysis of Bistatic Interferometer BAsed on Spaceborne SAR (BIBASS). As a bistatic system with general configuration, the system response of BIBASS is azimuth/range dependent. Taking into account this peculiarity, the appropriate theoretical framework is developed to make a more accurate evaluation of the performance of BIBASS. Firstly, the interferometric features are studied. Then, considering all kinds of de-correlation factors, a comprehensive investigation of coherence of such a system is conducted, followed by the relative height accuracy analysis. The theoretical analysis and simulation show that BIBASS, with the ability of high-precision height measurement, can be widely applied as a novel remote sensing measurement system.

1. INTRODUCTION

Bistatic Synthetic Aperture Radar (BSAR) has been researched as a hotspot in microwave imaging area during the last decade. Over the last few years, the BSAR synchronization and imaging technology have been studied well [1–6]. Several experiments with different topologies have been conducted, and a number of valuable results have been published [7–10]. Research is now moving towards the exploitation of BSAR application, including interferometric measurement and coherent change detection [11–14].

This paper proposes and discusses a particular sub-class of bistatic interferometric SAR configuration, where a spaceborne SAR, e.g., RADARSAT-2 or TerraSAR-X, is served as the transmitter of opportunity, while a fixed multi-channel receiver is mounted on a near-space platform, e.g., a stratospheric aerostat. After imaging and

---

Received 12 September 2013, Accepted 10 October 2013, Scheduled 14 October 2013

* Corresponding author: Qilei Zhang (zhangqilei1985@gmail.com).

interferometric process, this innovative remote sensing measurement system could be able to obtain the Digital Elevation Model (DEM) product with high-precision. The proposed system is named as Bistatic Interferometer BAsed on Spaceborne SAR, BIBASS [15].

Usually, the revisit cycle of spaceborne SAR is quite long (several days or more), and this system could only work for several seconds during the revisit [7, 8]. Therefore, to avoid echo window synchronization issues and to enhance the reliability of experiments, a conservative continuous data acquisition mode is applied in BIBASS. This means that the receiver is operated to acquire data continuously during the revisit of the spaceborne SAR, and the data processing could be done after the data acquisition. Moreover, since the velocity of the SAR satellite is much higher than that of the stratospheric aerostat, if the traditional stripmap mode is applied, the footprint overlapping would be very short and the beam synchronization would be very difficult. To overcome this, the wide-beam receiving mode could be applied in BIBASS. This means that the receiving beam of BIBASS should be wide enough to cover the observing scene and keep stationary. The problem of beam synchronization can be effectively resolved by choosing this kind of receiving mode.

As a passive single-pass interferometric system, BIBASS benefits from flexibility, low-cost, wide-swath, low temporal decorrelation and reliability [16]. This enables that BIBASS will be widely applied in the future missions. To verify and evaluate the concept of BIBASS, it is necessary to analyze the performance of this system. Furthermore, the analysis results could be used to guide and to optimize the system design.

For the traditional interferometric SAR (InSAR) system, the analysis theory of system performance has been established based on the mono-static SAR imaging geometry, in which mainly the interferometric pattern along the line of sight (LOS) was considered [17–21]. The coherence and height measurement performance of the distributed InSAR was analyzed by using the above-mentioned theory in [22]. Considering the particular geometric configuration, [23] analyzed the decorrelation factors and evaluated the relative height measurement performance of spaceborne distributed InSAR. For the latest TanDEM-X system, [11, 24, 25] analyzed the decorrelation factors and evaluated the interferometric performance.

However, as a bistatic system with general configurations, the response of BIBASS is azimuth/range dependent. Thus the interferometric feature of BIBASS is quite different from that of the traditional InSAR. In particular, the traditional InSAR can be treated as a special case of BIBASS. Therefore, this paper intends to develop an appropriate theoretical framework to analyze the interferometric performance of BIBASS.

The paper is organized as following. In Section 2, the system concept is presented and the interferometric features are derived and analyzed. Considering all kinds of de-correlation contributions, a comprehensive investigation of the performance of such a system, including the coherence and the relative height accuracy, is conducted in Section 3. Section 4 presents the performance of BIBASS by conducting simulation. At last, some conclusions are given in Section 5.

2. SYSTEM CONCEPT AND INTERFEROMETRIC FEATURES

2.1. System Concept

Figure 1 shows the system concept and the geometry configuration of BIBASS. As illustrated in Figure 1(a), BIBASS comprises the spaceborne SAR as transmitters of opportunity, while the receiver could be mounted on a fixed stratospheric aerostat.

As shown in Figure 1(b), the master receiver antenna A_1 and the slave receiver antenna A_2 are located in the plane ZOY, the height of A_1 is H. The baseline defined as the distance between A_1 and A_2 is B. The angle between the baseline and the Z axis is α. For arbitrary point P_0 with coordinate $(x,\, y,\, h)$ in the scene, the distances from it to A_1 and A_2 are r_1 and r_2,

$$r_1 = \sqrt{(H-h)^2 + x^2 + y^2} \tag{1}$$

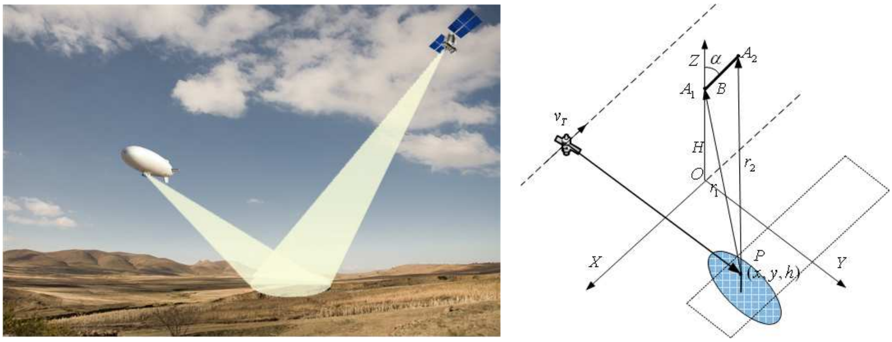

(a) (b)

Figure 1. The Bistatic Interferometer BAsed on Spaceborne SAR (BIBASS). (a) System concept. (b) Geometry configuration.

$$r_2 = \sqrt{(H + B\cos\alpha - h)^2 + x^2 + (y - B\sin\alpha)^2} \tag{2}$$

Then the parallax between r_1 and r_2 can be given as

$$\Delta r = r_2 - r_1 \approx B(\cos\beta\cos\alpha - \sin\gamma\sin\alpha) \tag{3}$$

where β and γ are the look angles of the point scatter P_0 for the master antenna A_1

$$\cos\beta = \frac{H-h}{r_1}; \quad \sin\gamma = \frac{y}{r_1} \tag{4}$$

Therefore, the interferometric phase corresponding to P_0 is

$$\phi = \frac{2\pi}{\lambda} \cdot \Delta r \approx \frac{2\pi}{\lambda} \cdot B(\cos\beta\cos\alpha - \sin\gamma\sin\alpha) \tag{5}$$

From (5), we can see that the interferometric phase is related to the geometry configuration and the coordinate of the target. Therefore, with the knowledge of the geometry configuration and the planar coordinate, i.e., (x, y), we can be able to obtain the height information h of the target by processing the interferometric phase. This is the principle of the height measurement for BIBASS.

2.2. Interferometric Features

For the conventional InSAR system, the interferogram usually consists of a dominant trend in the range direction, referred as the phase generated by an ideally flat Earth, and some 'distorted' pattern which is caused by terrain height variations [17]. However, for BIBASS, it is necessary to investigate the interferogram trend along three directions, namely, azimuth, range and height directions. The reason for this is that three-dimensional height measurement geometry is applied in BIBASS.

To investigate the character of the interferogram of BIBASS, another point P_1, which is located nearby P_0, is introduced. Assuming that the coordinate of P_1 is (x', y', h'), the corresponding look angles are β' and γ', then the interferometric phase variation between P_1 and P_0 can be expressed as

$$\Delta\phi \approx -\frac{2\pi}{\lambda} B(\cos\alpha\sin\beta\delta\beta + \sin\alpha\cos\gamma\delta\gamma) \tag{6}$$

where, $\delta\beta = \beta - \beta'$, $\delta\gamma = \gamma - \gamma'$. Figure 2 shows three different geometric positions of P_1. In each case, only the coordinate variation in one direction is considered, with other two coordinates fixed. It is worth to pointing out that the range discussed in this paper is referred as the slant range.

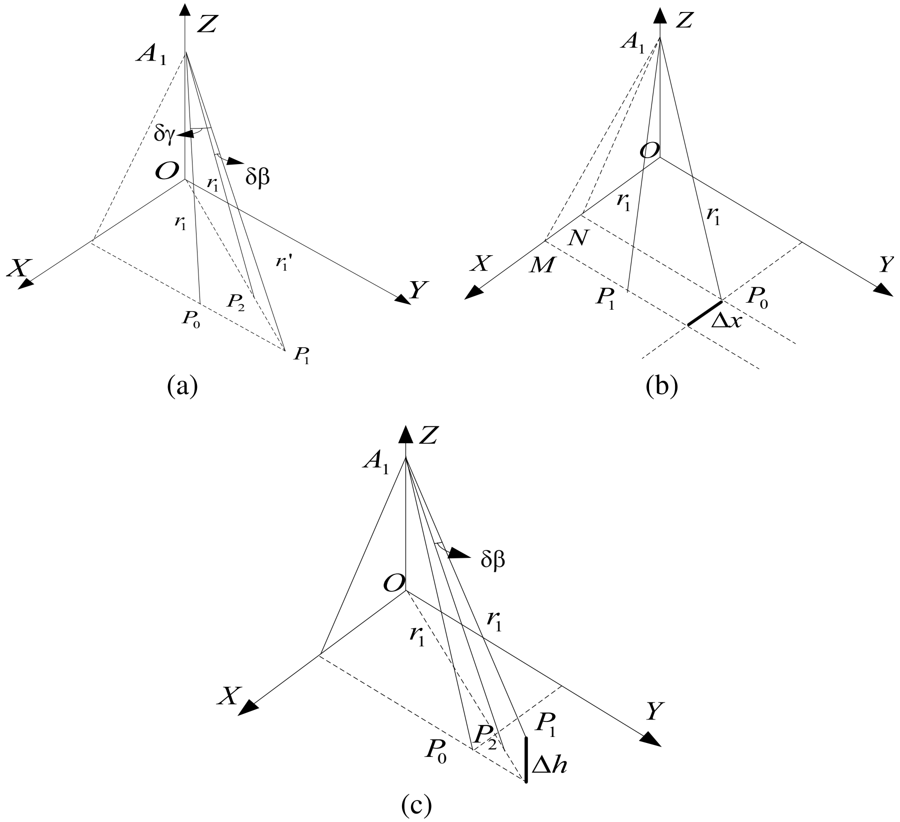

Figure 2. Position variations along three directions. (a) Range variation. (b) Azimuth variation. (c) Height variation.

2.2.1. Interferogram due to the Range Variation

As sketched in Figure 2(a), assuming that P_1 and P_0 only have the position variation in range directionand the distance from P_1 and P_0 to A_1 are r_1 and r_1', thus $\angle P_1A_1P_0 = \delta\gamma$. Moreover, assuming that the distance from P_2 to A_1 is r_1, thus $\angle P_1A_1P_2 = \delta\beta$. According to the geometry shown in Figure 2(a), letting $R = \frac{r_1+r_1'}{2}, \Delta R = r_1' - r_1$, we can get:

$$\begin{aligned} R\cdot\delta\beta &\approx R\cdot\sin\delta\beta = \frac{\Delta R}{\tan\beta} \\ R\cdot\delta\gamma &\approx R\cdot\sin\delta\gamma = \frac{\Delta R}{\tan\gamma} \end{aligned} \tag{7}$$

Substituting (7) into (6), the interferometric phase variation caused by the range variation can be obtained:

$$\Delta\phi_r \approx -\frac{2\pi}{\lambda} \cdot \frac{B}{R} \cdot \left(\cos\alpha\cos\beta + \sin\alpha\frac{\cos\gamma}{\tan\gamma}\right) \cdot \Delta R \tag{8}$$

2.2.2. Interferogram due to the Azimuth Variation

As sketched in Figure 2(b), supposing that the range from P_1 and P_0 to A_1 are the same and that the only position offset between P_1 and P_0 is the azimuth variation Δx, thus according to (4), we can get that $\delta\beta = 0$. Then, $\angle P_0 A_1 N = \gamma$, $\angle P_1 A_1 M = \gamma'$. Letting $R = r$, we can get

$$\delta\gamma \approx -\frac{\sin\theta_0}{R\sin\gamma} \cdot \Delta x \tag{9}$$

where $\sin\theta_0 = \frac{x}{\sqrt{H^2+x^2}}$. Therefore, substituting (9) into (6), the interferometric phase variation caused by the azimuth variation can be obtained as

$$\Delta\phi_a \approx \frac{2\pi}{\lambda} \cdot \frac{B\sin\alpha\sin\theta_0}{R\tan\gamma} \cdot \Delta x \tag{10}$$

2.2.3. Interferogram due to the Height Variation

As shown in Figure 2(c), we assume that the range from P_1 and P_0 to A_1 are the same, and the only position offset between P_1 and P_0 is the height variation Δh. Supposing that the distance from P_2 to A_1 is r_1 as well, thus $\angle P_1 A_1 P_2 = \delta\beta$. According to the geometry in Figure 2(c) and letting $R = r$, we can obtain

$$\begin{gathered} R \cdot \delta\beta \approx R \cdot \sin\delta\beta = \frac{\Delta h}{\sin\beta} \\ \delta\gamma \approx \frac{\cos\theta_0}{R\sin\gamma} \cdot \Delta h \end{gathered} \tag{11}$$

where $\cos\theta_0 = \frac{H}{\sqrt{H^2+x^2}}$. Therefore, the interferometric phase variation caused by the height variation can be derived as

$$\Delta\phi_h = -\frac{2\pi}{\lambda} \cdot \frac{B}{R} \cdot \left(\cos\alpha + \frac{\sin\alpha\cos\theta_0}{\tan\gamma}\right) \cdot \Delta h \tag{12}$$

2.3. Interferometric Parameters

Based on the derived results, we can calculate the key interferometric parameters of BIBASS, namely, the local fringe frequency (LFF) and the height of ambiguity (HoA) [19, 20]. The LFF represents the flat earth phase effect, while the HoA represents the height sensitivity of the interferometer [17]. Unlike conventional InSAR systems, the response of BIBASS is azimuth/range dependent. Therefore, the LFF of BIBASS consists of two components: range LFF and azimuth LFF. Moreover, the HoA of BIBASS is azimuth/range dependent as well.

$$f_r = \frac{1}{2\pi}\frac{\delta\phi_r}{\delta R} = -\frac{B}{\lambda R}\cdot\left(\cos\alpha\cos\beta + \sin\alpha\frac{\cos\gamma}{\tan\gamma}\right) \tag{13}$$

$$f_a = \frac{1}{2\pi}\frac{\delta\phi}{\delta x} = \frac{B\sin\alpha\sin\theta_0}{\lambda R\tan\gamma} \tag{14}$$

$$h_{amb} = \frac{\lambda R}{B\left(\cos\alpha + \frac{\sin\alpha\cos\theta_0}{\tan\gamma}\right)} \tag{15}$$

The calculated interferometric parameters of BIBASS are plotted in Figure 3. The parameters used in the calculation are listed in Table 1. It can be seen from Figure 3(a) that the range LFF decreases as the receiver-to-target range (the detected range) increases, as expected, and the range LFF (phase-to-range sensitivity) at scene edge is higher than that at scene center. It can also be observed from Figure 3(b) that the azimuth LFF is symmetrical and increases with the absolute azimuth coordinate value. The calculated result shown in Figure 3(b) suggests that the azimuth LFF (phase-to-azimuth sensitivity) is weakly dependent on the detected range. For the phase-to-height sensitivity, we can see from Figure 3(c) that the HoA increases linearly with the detected ting range. This implies that the phase-to-height sensitivity goes down as the detected range rises. Meanwhile, we can also find that the HoA at scene edge is slightly higher than that at scene center. Overall, the interferometric phase sensitivity of BIBASS declines as the detected range rises, meanwhile, the flat earth effect increases and the phase-to-height sensitivity decreases as the azimuth offset increases.

It should be pointed out that, along the scene central line, $\sin\theta_0 = 0$, $\cos\theta_0 = 1$, and $\beta = \gamma$, thus $f_a = 0$, $f_r = -\frac{B}{\lambda R}\cdot\frac{\sin(\alpha+\beta_0)}{\tan\beta_0}$, $h_{amb} = \frac{\lambda R}{B}\cdot\frac{\sin\beta_0}{\sin(\alpha+\beta_0)}$, where $\beta_0 = \arcsin(\frac{y}{\sqrt{(H-h)^2+y^2}})$. These are the interferometric parameters of the conventional mono-static InSAR. The reason for this is that, in this case, the geometric configuration of BIBASS degrades to the conventional mono-static SAR. Therefore, mono-static InSAR can be treated as a special case of BIBASS.

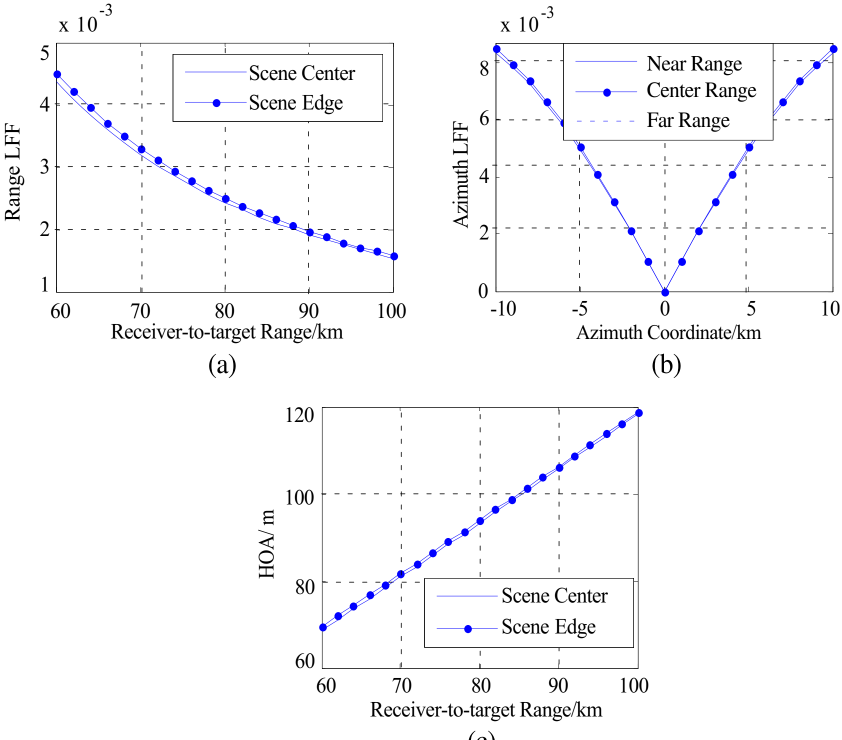

(a)

(b)

(c)

Figure 3. The interferometric parameters of BIBASS. (a) Range LFF. (b) Azimuth LFF. (c) Height of Ambiguity.

3. COHERENCE AND RELATIVE HEIGHT ACCURACY

The key performance quantity of interferometric systems is the coherence, which is the dominant factor of the relative height accuracy [11, 17]. This section presents a comprehensive analysis of the coherence of BIBASS, followed by the discussion of the relative height accuracy. The presented different decorrelation factors include limited signal-to-noise ratio (SNR), spatial baseline, volume scattering, ambiguities, quantization, co-registration error and synchronization error.

3.1. SNR Decorrelation

The SNR decorrelation is due to the reality of finite signal-to-noise ratio (SNR) of BIBASS. Assuming that the SNR of two images is same, and then the de-correlation effect caused by SNR can be rewritten as [17]

$$\gamma_{SNR} = \frac{1}{1 + SNR^{-1}} \tag{16}$$

According to the radar equation of the bistatic SAR [26], the SNR of BIBASS can be given as:

$$SNR = \frac{P_{av} G_T G_R \lambda^2 \sigma T_{int}}{(4\pi)^3 R_T^2 R_R^2 K_B T_S F L} \tag{17}$$

where P_{av} is the average transmitter power, λ the wavelength, σ the bistatic radar cross section, T_{int} the synthetic aperture time, K_B the Boltzmann constant, T_S the receiver temperature, F the noise figure, L the system loss, G_T (or G_R) the antenna gain of the transmitter (or the receiver), and R_T (or R_R) the range from the transmitter (or the receiver) to the target, respectively. Due to the reality that the receiver-to-target range of BIBASS is much shorter than that of spaceborne SAR, and the fine SNR performance is one of the advantages for BIBASS.

3.2. Spatial Decorrelation

Spatial de-correlation is due to the slightly different viewing angle between two data acquisition geometries [18, 21]. As shown in Figure 1, the viewing angle offset is caused by the baseline between A_1 and A_2. The system response of BIBASS is azimuth/range dependent. Therefore, a theoretical model of spatial decorrelation should be established with considering this peculiarity. In the case of pure surface scattering, this section establishes the spatial decorrelation model.

Figure 4 shows the imaging geometry of BIBASS to be used in this analysis. It is convenient to establish the coordinate system in such a way that O is at the coordinate origin, and the XOY plane coincides with the ground plane. The point $P(x_0, y_0)$ is the center of a resolution cell in the imaging scene. The distances from $P(x_0, y_0)$ to A_1 and A_2 are $r_1(x_0, y_0)$ and $r_2(x_0, y_0)$, respectively. As sketched in Figure 4, the point $P'(x, y)$ is in the vicinity of P, i.e., it is a point scatterer within the resolution cell. The distances from $P'(x, y)$ to A_1 and A_2 are $r_1(x, y)$ and $r_2(x, y)$, respectively.

Based on the point scattering model, the complex bistatic SAR image signal without the system thermal noise measured by the antennas A_1 and A_2 can be represented as the sum of complex returns of all the point scatterers within the resolution cell:

$$s_i = \iint \sigma_b(x, y) \exp\left(-j\frac{2\pi}{\lambda}(r_T + r_i(x, y))\right) \cdot W(x, y) dx dy, \quad i = 1, 2 \tag{18}$$

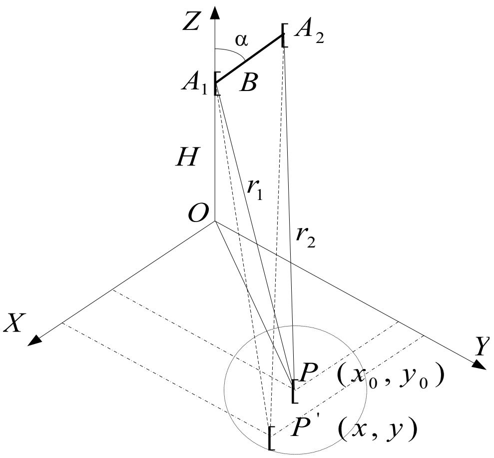

Figure 4. The imaging geometry of BIBASS.

where σ_b denotes the complex bistatic backscatter coefficient at each point on the plane, λ the wavelength, and $W(x, y)$ the point spread function (PSF) of BIBASS. The PSF of BIBASS can be expressed as:

$$W(x, y) = \sin c\left((x - x_0)/\rho_x\right) \cdot \sin c\left((y - y_0)/\rho_y\right) \tag{19}$$

where $\sin c(x) = \sin(\pi x)/\pi x$, and ρ_x and ρ_y are the azimuth resolution and range resolution, respectively.

The correlation coefficient of these two images, indicating the coherence loss caused by spatial baseline, can be given as

$$\gamma_{Spatial} = \left| \frac{\langle S_1 S_2^* \rangle}{\sqrt{\langle S_1 S_1^* \rangle \langle S_2 S_2^* \rangle}} \right| \tag{20}$$

After the co-registration of the master and the slave images, applying interferometric process will yield

$$\begin{aligned} S_1 S_2^* = &\iiiint \sigma_0(x, y) \sigma_0^*(x', y') \exp\left(-j \frac{2\pi}{\lambda}(r_0(x, y) + r_1(x, y))\right) \\ &\operatorname{sinc}\left(\frac{x - x_0}{\rho_x}\right) \operatorname{sinc}\left(\frac{y - y_0}{\rho_y}\right) \cdot \exp\left(j \frac{2\pi}{\lambda}(r_0(x', y') + r_2(x', y'))\right) \\ &\sin c\left(\frac{x' - x_0}{\rho_x}\right) \sin c\left(\frac{y' - y_0}{\rho_y}\right) dx dy dx' dy' \end{aligned} \tag{21}$$

Assuming that the imaged surface consists of uniformly distributed and uncorrelated scattering centers [18],

$$\left\langle \sigma_0(x, y) \cdot \sigma_0^*(x', y') \right\rangle = \sigma_0^2 \cdot \delta(x - x', y - y') \tag{22}$$

where $\langle\cdot\rangle$ indicates the assemble average, then (22) can be reduced into

$$\begin{aligned}\left\langle S_1 S_2^*\right\rangle &= \iint \sigma_0^2 \exp\left(-j\frac{2\pi}{\lambda}(r_1(x,y)-r_2(x,y))\right)\\ &\quad \sin c^2\left(\frac{x-x_0}{\rho_x}\right)\sin c^2\left(\frac{y-y_0}{\rho_y}\right)dxdy \end{aligned}\tag{23}$$

According to the geometry relation between $P'(x,y)$ and $P(x_0,y_0)$ shown in Figure 4, we can obtain

$$\begin{cases} r_1(x,y)\approx r_1(x_0,y_0)+(y-y_0)\sin\theta_1+(x-x_0)\sin\varphi_1\\ r_2(x,y)\approx r_2(x_0,y_0)+(y-y_0)\sin\theta_2+(x-x_0)\sin\varphi_2\end{cases}\tag{24}$$

where

$$\begin{aligned}\sin\theta_1 &= \frac{y_0}{\sqrt{H^2+x_0^2+y_0^2}}\\ \sin\varphi_1 &= \frac{x_0}{\sqrt{H^2+x_0^2+y_0^2}}\\ \sin\theta_2 &= \frac{y_0-B\sin\alpha}{\sqrt{(H+B\cos\alpha)^2+x_0^2+(y_0-B\sin\alpha)^2}}\\ \sin\varphi_2 &= \frac{x_0}{\sqrt{(H+B\cos\alpha)^2+x_0^2+(y_0-B\sin\alpha)^2}}\end{aligned}\tag{25}$$

Combining (24) and (25) suggests that the phase term in the integral of (23) is the linear function of variables x and y. This implies that this term can be seen as the Fourier Transform kernel. Therefore, the interferometric model of BIBASS can be derived by applying Fourier Transform features.

$$\begin{aligned}\left\langle S_1 S_2^*\right\rangle &= \sigma_0^2\rho_x\rho_y \exp\left(-j\frac{2\pi}{\lambda}(r_1(x_0,y_0)-r_2(x_0,y_0))\right)\\ &\quad\times\left(1-\frac{\cos\theta\,|\delta\theta|}{\lambda}\rho_y\right)\left(1-\frac{\cos\varphi\,|\delta\varphi|}{\lambda}\rho_x\right)\end{aligned}\tag{26}$$

where $\theta=\frac{\theta_1+\theta_2}{2}, \delta\theta=\theta_1-\theta_2$; $\varphi=\frac{\varphi_1+\varphi_2}{2}, \delta\varphi=\varphi_1-\varphi_2$. Based on the geometry configuration shown in Figure 4, we can also get

$$\begin{aligned}\delta\theta &\approx \frac{\sin\theta\cos\theta_0\cos\alpha+\cos\theta\sin\alpha}{\sqrt{H^2+x_0^2+y_0^2}}\cdot B\\ \delta\varphi &\approx \frac{\sin\varphi\cos(\varphi_0-\alpha)}{\sqrt{H^2+x_0^2+y_0^2}}\cdot B\end{aligned}\tag{27}$$

where

$$\cos\theta_0=\frac{H}{\sqrt{H^2+x_0^2}};\quad \cos\varphi_0=\frac{H}{\sqrt{H^2+x_0^2+y_0^2}}\tag{28}$$

The auto-correlation of them can be given by [19]

$$\langle S_1 S_1^* \rangle = \langle S_2 S_2^* \rangle = \sigma_0^2 \rho_x \rho_y \tag{29}$$

From (26) and (29), we can get the spatial decorrelation:

$$\begin{aligned}\gamma_{Spatial} &= \left(1 - \left|\frac{\cos\theta\rho_y}{\lambda} \cdot \frac{\sin\theta\cos\theta_0\cos\alpha + \cos\theta\sin\alpha}{R_0} \cdot B\right|\right) \\ &\quad \times \left(1 - \left|\frac{\cos\varphi\rho_x}{\lambda} \cdot \frac{\sin\varphi\cos(\varphi_0 - \alpha)}{R_0} \cdot B\right|\right)\end{aligned} \tag{30}$$

where $R_0 = \sqrt{H^2 + x_0^2 + y_0^2}$. We can see from (30) that the spatial decorrelation of BIBASS can be decomposed into two components along range direction and along the azimuth direction. The range spatial decorrelation component indicated by the first term in (30) is similar to the spatial decorrelation contribution for the conventional InSAR system. However, the azimuth spatial decorrelation component represented by the second term in (30) is quite particular, since the impact of this component is dependent on the azimuth position. In particular, the effect of azimuth spatial decorrelation is zero at scene central line, since $\varphi = 0$; the effect increases with the azimuth position offset, and achieve the maximum value at the scene edge. This is consistent with the conclusion given in the last section, i.e., the monostatic InSAR can be treated as a special case of BIBASS.

3.3. Volume Scattering Decorrelation

For the vegetated area, it is necessary to analyze the coherence loss due to the volume scattering. The principle of the volume scattering decorrelation is similar to the above-mentioned spatial decorrelation. The existence of multiple scatterers with different height within a single resolution cell results in the increase of the interferometric phase uncertainty, and then the coherence loss of the interferogram [17]. The decorrelation effect of the volume scattering can be expressed as

$$\gamma_{Vol} = \frac{\left|\int\limits_0^{h_v} \rho(z)\exp\left(j2\pi\frac{z}{h_{amb}}\right)dz\right|}{\int\limits_0^{h_v} \rho(z)dz} \tag{31}$$

where h_{amb} is the HoA given by (15), h_v is the vegetation height, and $\rho(z)$ is the vertical scattering profile.

Taking into account the extinction in a homogeneous medium, the random volume (RV) model is an appropriate model of structure function for the vegetated area [27]. Moreover, considering the difference between the incident angle and the reflected angle in bistatic SAR configurations, the vertical scattering profile should be rewritten as

$$\rho(z) = \varepsilon_v \cdot \exp\left[-\kappa_e \cdot \left(\frac{h_v - z}{\cos\theta_T} + \frac{h_v - z}{\cos\theta_R}\right)\right], \quad 0 \leq z \leq h_v \tag{32}$$

where ε_v is a constant; however, it will be omitted in the calculation. κ_e is the one-way amplitude extinction coefficient in Nepers per meter [11], and $\cos\theta_T$ and $\cos\theta_R$ are the incident angle and the reflected angle, respectively.

By instituting (32) into (31) yields

$$\gamma_{Vol} = \left|\frac{\xi_1}{\xi_1 + \xi_2} \cdot \frac{\exp\left[\xi_2 \cdot h_v\right] - \exp\left[-\xi_1 \cdot h_v\right]}{1 - \exp\left[-\xi_1 \cdot h_v\right]}\right| \tag{33}$$

where

$$\xi_1 = \kappa_e \cdot \frac{\cos\theta_T + \cos\theta_R}{\cos\theta_T \cos\theta_R}; \quad \xi_2 = j\frac{2\pi}{h_{amb}} \tag{34}$$

3.4. Other Decorrelation Factors

Beside the above mentioned decorrelation sources, other decorrelation factors have to be analyzed for BIBASS.

In SAR system, the value of ambiguity signal is represented by the Ambiguity-to-Signal Ratio (ASR), which is defined by the ratio between the ambiguity signal and the expected signal [28]. The ASR can be decomposed into the Range Ambiguity-to-Signal Ratio (RASR) and the Azimuth Ambiguity-to-Signal Ratio (AASR). The coherence loss caused by the ASR can be given as

$$\gamma_{Amb} = \frac{1}{1 + \mathrm{RASR}} \cdot \frac{1}{1 + \mathrm{AASR}} \tag{35}$$

Another decorrelation source is the quantitation error resulting from the limited number of bits used for digital representation of the recorded echo. As a comparison of the complexity and the performance, usually, the quantitation level for spaceborne SAR is 3 or 4, with the corresponding coherence loss 0.946 or 0.989 [29]. However, the downlink capability of BIBASS is abundant, since the revisit cycle of spaceborne transmitter is several days. Therefore, the higher quantitation level can be applied, and the corresponding coherence loss is ignorable.

The coregistration error will result in not only the interferometric phase offset, but also the coherence loss [30]. Assuming that the azimuth coregistration error is Δx, and the range coregistration error is Δy, then the decorrelation effect can be expressed as

$$\gamma_{\Delta x} = \sin c\left(\frac{\pi\Delta x(1 - |Bk_x/\lambda R|)}{\rho_x}\right) \tag{36}$$

$$\gamma_{\Delta y} = \sin c\left(\frac{\pi\Delta y(1 - |Bk_y/\lambda R|)}{\rho_y}\right) \tag{37}$$

where $k_x = \cos\varphi\sin\varphi\cos(\varphi_0 - \alpha)\rho_x$, $k_y = \cos\theta(\sin\theta\cos\theta_0\cos\alpha + \cos\theta\sin\alpha)\rho_y$. Generally, the requirement of SAR interferometric application is that the coregistration error is smaller than 0.1 pixels.

Since the transmitter and the receiver are separated, the decorrelation effect of the space, time and frequency synchronization errors should be taken into account in BIBASS.

The space synchronization (beam synchronization) error will result in the degradation of the system SNR, and then the coherence loss between consecutive images. However, as mentioned above, the problem of beam synchronization can be effectively resolved by applying the wide-beam receiving mode. Therefore, the corresponding coherence loss can be ignored.

The time and frequency synchronization errors are caused by the independent oscillators used in the separated transmitter and receiver. This will result in the range measurement error and the phase error, and then impact the imaging result and the interferometric application. The time and frequency synchronization error consists of the deterministic component and the random component. However, the same local oscillator is used in the receiver subsystem of BIBASS. This means that the deterministic synchronization error will not result in the coherence loss, since it can be eliminated by the interferometric process. Assuming that the random phase error resulting from the time and frequency synchronization error are ϕ_{nt} and ϕ_{nf} with the mean variance σ_{nt} and σ_{nf}, where $n = 1, 2$ represent the master and the slave images, the corresponding decorrelation contribution can be expressed by [31]

$$\gamma_{Syn} = \exp\left[-\left(\sigma_{1t}^2 + \sigma_{1f}^2 + \sigma_{2t}^2 + \sigma_{2f}^2\right)/2\right] \tag{38}$$

According to the performance of the current oscillator, the impact of the random synchronization error on the coherence loss can also be ignored [32]. However, what we need to highlight here is that the random synchronization error will result in a residual interferometric phase, which will be discussed in the following discussion.

3.5. Relative Height Accuracy

The total coherence γ_{Tot} of BIBASS can be calculated by multiplying the above-mentioned decorrelation factors. Then the estimation error of the interferometric phase can be derived, followed by the calculation of the relative height accuracy of BIBASS. Assuming that the number of the independent looks is L, then the probability density function (PDF) of the interferometric phase can be given by [33]:

$$\begin{aligned} p_\varphi(\varphi) \ = \ & \frac{\Gamma(L+\frac{1}{2})(1-|\gamma_{Tot}|^2)^L\,|\gamma_{Tot}|\cos(\varphi-\varphi_0)}{2\sqrt{\pi}\Gamma(L)(1-|\gamma_{Tot}|^2\cos^2(\varphi-\varphi_0))^{L+1/2}} \\ & +\frac{(1-|\gamma_{Tot}|^2)^L}{2\pi}F\left(L,1;\frac{1}{2};|\gamma_{Tot}|^2\cos^2(\varphi-\varphi_0)\right) \end{aligned} \quad (39)$$

where φ_0 is the true value of the interferometric phase φ, $\Gamma(\cdot)$ the Gamma function, and $F(\cdot)$ the Gaussian hyper-geometric function. Letting $\Delta\varphi = \varphi - \varphi_0$ be the estimation error of the interferometric phase, the standard variance of $\Delta\varphi$ is given by

$$\sigma_{\Delta\varphi} = \sqrt{\int_{-\pi}^{\pi}(\varphi-\varphi_0)^2 p_\varphi(\varphi)d\varphi} \quad (40)$$

Equation (40) indicates the estimation accuracy of the interferometric phase. Moreover, taking into account the interferometric phase error caused by the residual synchronization error, the relative height measurement accuracy can be written by

$$\Delta h = h_{amb}\cdot(\Delta\varphi/2\pi) \quad (41)$$

where $\Delta\varphi = \sigma_{\Delta\varphi} + \Delta\varphi_{Syn}$, $\Delta\varphi_{Syn}$ is the interferometric phase error resulting from the residual synchronization error.

4. SIMULATION ANALYSIS

Based on the above derived theory, this section analyzes the performance of BIBASS by conducting simulation. The simulation parameters are listed in Table 1. The transmitter's parameters are related to the C-band spaceborne SAR system-RADARSAT-2, which was launched in December 2007 [34].

Assuming that the height of the receiver's platform (stratospheric aerostat) is 20 km, the distance from the receiver to the scene center is 80 km, and the imaged scene size is 20 km × 20 km, thus the beam width of the receiver's antenna needs to be 14.32° (Horizontal) and 3.58° (Elevation), and then the corresponding aperture of the receiver's antenna is 0.22 m and 0.89 m (C-band, $\lambda = 5.6\,\text{cm}$).

Table 1. Simulation parameters of BIBASS.

Parameters	**Value**	**Parameters**	**Value**
Carrier frequency	5.405 GHz	Aerostat Height	20 km
Bandwidth	30 MHz	Receiver Antenna Length	0.22 m
Satellite Height	798 km	Receiver Antenna Width	0.89 m
Average Transmitter Power	300 W	Sampling Frequency	50 MHz
Noise Figure + Loss	5 dB	Receiver-to-Target Range	60–100 km
Transmitter Antenna Length	15 m	Scene Length	20 km
Transmitter Antenna Width	1.5 m	Scene Width	20 km
Incident Angle	35 deg	Target RCS	2 m^2
Baseline length	50 m	Baseline Obliquity	30 deg

Figure 5 shows different decorrelation sources of BIBASS. The decorrelation effect of SNR is shown in Figure 5(a), where three beams were used to cover a 40 km swath, and the used antenna pattern is $\sin c^2$. We can find that the coherence goes down with the detected range goes up, since the SNR decreases as the detected range. However, the coherence loss of BIBASS due to finite SNR is smaller than 0.05 for the whole covered scene. Figure 5(b) illustrates the spatial decorrelation. From this we can see that the decorrelation effect caused by spatial baseline decreases with the detected range. The coherence at the scene edge is better than that at the scene center. This is consistent with the derived result shown by (30). The coherence loss caused by the volume scattering is shown in Figure 5(c). In the calculation, we assume that $\kappa_e = 1\,\mathrm{dB/m}$ [11], and the reflected angle is $\theta_R = 76^\circ$, which is corresponding to the detected range is 80 km. We can conclude that the coherence climbs as the HoA increases. We can also find that the decorrelation effect increases with the vegetation height, however, the trend of this is getting slow with the increase of the vegetation height. Figure 5(d) shows the coherence loss caused by the signal ambiguities. We can find that the decorrelation effect of ASR is dependent on the Pulse Repetition Frequency (PRF), but weakly dependent on the detected range. It's worth pointing out that, for BIBASS, the effect of RASR is much smaller than that of the AASR.

Taking into account all kinds of decorrelation factors mentioned above, the total coherence of BIBASS operating with the parameters listed in Table 1 is illustrated in Figure 6, in which the solid line indicates the performance at the scene center, while the dotted line indicates the performance at the scene edge. In the calculation, PRF = 1000 Hz, and the vegetation height is 10 m. We can see from Figure 6 that the total coherence of BIBASS is on the order of 0.88 to 0.95, and the coherence at the scene center is higher than that at the scene edge.

Assuming that the independent looks $L = 4$ and that the residual synchronization phase error is 5°, Figure 7 shows the interferometric phase error and the relative height accuracy of BIBASS, where the solid line indicates the performance at the scene center, while the dotted line indicates the performance at the scene edge. We can see from Figure 7 that for BIBASS operating with the parameters listed in Table 1, the interferometric phase error is lower than 0.32 rad and the relative height accuracy is better than 5 m. We can also find that the performance of BIBASS at scene center is better than that at the

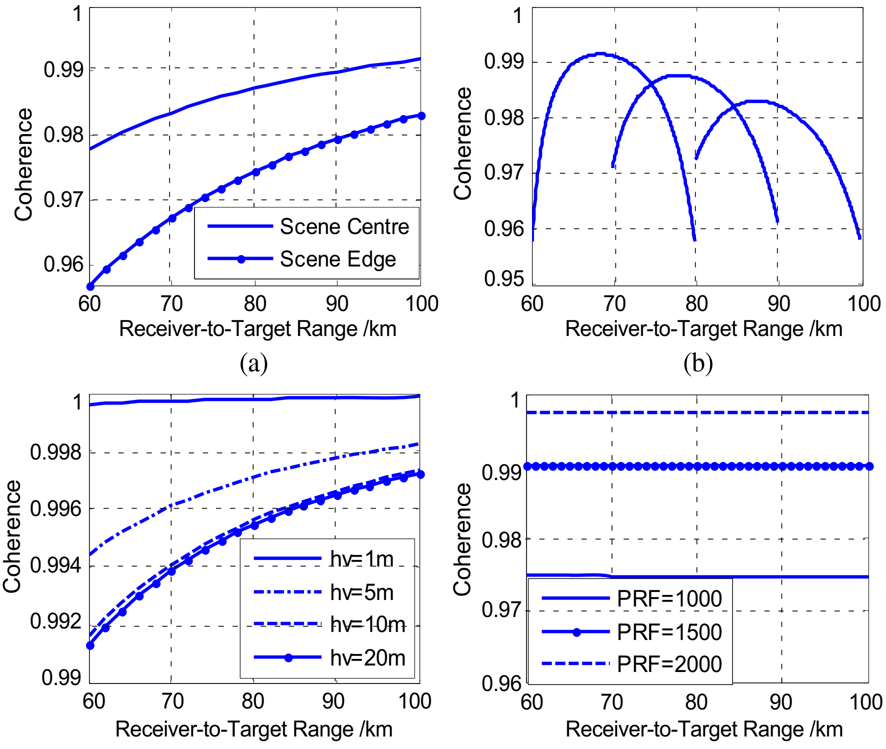

(a) (b) (c) (d)

Figure 5. Decorrelation sources of BIBASS. (a) SNR decorrelation. (b) Spatial decorrelation. (c) Volume scattering decorrelation. (d) Ambiguity decorrelation.

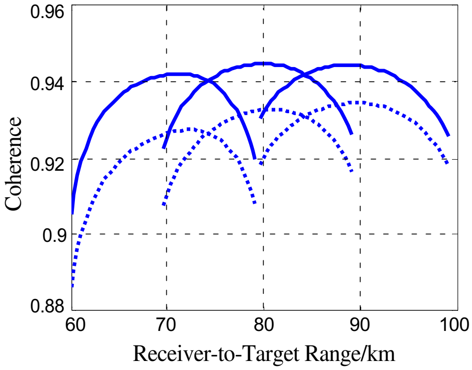

Figure 6. The total coherence of BIBASS.

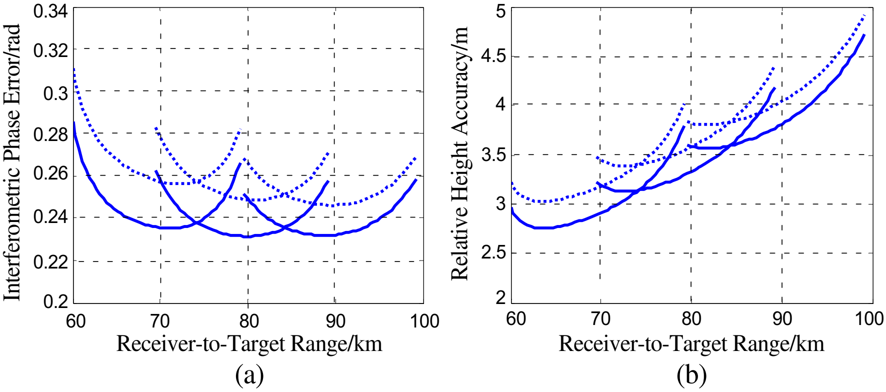

Figure 7. The interferometric phase error and relative height accuracy of BIBASS. (a) The interferometric phase error. (b) The relative height accuracy.

scene edge. Moreover, even though the estimation accuracy of the interferometric phase increases with the detected range, the relative height accuracy degrades as the detected range increases. The reason for this is that, as shown in Figure 3(c), the HoA increases quickly with the detected range.

From the simulated results and the discussion presented above, it is clear that, to improve the relative height accuracy, we need to decrease the impact of the spatial decorrelation and to reduce the residual synchronization phase error. The first one can be realized by performing pre-filtering, while the second one can be realized by applying more accurate synchronization method [27, 32].

5. CONCLUSIONS

This paper analyzes the performance of a particular bistatic interferometric system-Bistatic Interferometer BAsed on Spaceborne SAR (BIBASS). Firstly, the interferometric parameters of BIBASS are derived and analyzed based on the geometry configuration. Then, taking into account all decorrelation factors, a comprehensive analysis of the coherence performance is presented, followed by the discussion of the relative height accuracy. At last, the derived theory is also applied to analyze the performance of BIBASS by simulation. Both the derived theory and the simulated result suggest that BIBASS is able to obtain height measurement production with high-precision. The next step is to develop the system hardware and to conduct experimental investigation.

REFERENCES

1. Lopez-Dekker, P., J. J. Mallorqui, P. Srra-Morales, and J. Sanz-Marcos, "Phase synchronization and Doppler centroid estimation in fixed receiver bistatic SAR systems," *IEEE Trans. Geosci. Remote Sens.*, Vol. 46, 3459–3471, 2008.
2. He, Z., F. He, J. Li, H. Huang, Z. Dong, and D. Liang, "Echo-domain phase synchronization algorithm for bistatic SAR in alternating bistatic/ping–pong mode," *IEEE Geosci. Remote Sens. Lett.,* Vol. 9, 604–608, 2012.
3. Wang, W., "Approach of adaptive synchronization for bistatic SAR real-time imaging," *IEEE Trans. Geosci. Remote Sens.,* Vol. 45, 2695–2700, 2007.
4. Liu, Y., Y. Deng, R. Wang, and X. Jia, "Bistatic FMCW SAR raw signal simulator for extended scenes," *Progress In Electromagnetics Research*, Vol. 128, 479–502, 2012.
5. Qiu, X., D. Hu, and C. Ding, "An improved NLCS algorithm with capability analysis for one-stationary BiSAR," *IEEE Trans. Geosci. Remote Sens.*, Vol. 46, 3179–3186, 2008.
6. Wu, J., Z. Li, Y. Huang, and J. Yang, "Processing one-stationary bistatic SAR data using inverse scaled fourier transform," *Progress In Electromagnetics Research*, Vol. 129, 143–159, 2012.
7. Rodriguez-Cassola, M., S. V. Baumgartner, G. Krieger, and A. Moreira, "Bistatic TerraSAR-X/F-SAR spaceborne-airborne SAR experiment: Description, data processing, and results," *IEEE Trans. Geosci. Remote Sens.*, Vol. 48, 781–794, 2010.

8. Walterscheid, I., T. Espeter, A. R. Brenner, J. Klare, J. H. Ender, H. Nies, R. Wang, and O. Loffeld, "Bistatic SAR experiments with PAMIR and TerraSAR-X: Setup, processing and image results," *IEEE Trans. Geosci. Remote Sens.*, Vol. 48, 3268–3279, 2010.
9. Sanz-Marcos, J., P. Lopez-Dekker, J. J. Mallorqui, A. Aguasca, and P. Prats, "SABRINA: A SAR bistatic receiver for interferometric applications," *IEEE Geosci. Remote Sens. Lett.*, Vol. 4, 307–311, 2007.
10. Antoniou, M., Z. Zeng, F. Liu, and M. Cherniakov, "Experimental demonstration of passive BSAR imaging using navigation satellites and a fixed receiver," *IEEE Geosci. Remote Sens. Lett.*, Vol. 9, 477–481, 2012.
11. Krieger, G., A. Moreira, H. Fiedler, I. Hanjnsek, M. Werner, M. Younis, and M. Zink, "TanDEM-X: A satellite formation for high-resolution SAR interferometry," *IEEE Trans. Geosci. Remote Sens.*, Vol. 45, 3317–3341, 2007.
12. Duque, S., P. Lopez-Dekker, J. J. Mallorqui, and J. C. Merlano, "Repeat-pass interferometry using a fixed-receiver and ERS-2/ENVIST as transmitters of opportunity," *Proceedings of IEEE Geoscience Remote Sensing Symposium*, 246–249, Cape Town, South Africa, 2009.
13. Duque, S., P. Lopez-Dekker, and J. J. Mallorqui, "Single-pass bistatic SAR interferometry using fixed-receiver configurations: Theory and experimental validation," *IEEE Trans. Geosci. Remote Sens.*, Vol. 48, 2740–3749, 2010.
14. Liu, F., M. Antoniou, Z. Zeng, and M. Cherniakov, "Coherent change detection using passive GNSS-based BSAR: Experimental proof of concept," *IEEE Trans. Geosci. Remote Sens.*, Vol. 51, 4544–4555, 2013.
15. Zhang, Q., W. Chang, and F. Yan, "Bistatic interferometer based on spaceborne SAR," *Proceedings of IET International Radar Conference*, Xi'an, China, 2013.
16. Wang, W., J. Cai, and Q. Peng, "Near-space microwave radar remote sensing: Potentials and challenge analysis," *Remote Sens.*, Vol. 2, 717–739, 2010.
17. Bamler, R. and P. Hartl, "Synthetic aperture radar interferometry," *Inverse Problems.*, Vol. 14, 1–54, 1998.
18. Zebker, H. A. and J. Villasenor, "Decorrelation in interferometric radar echoes," *IEEE Trans. Geosci. Remote Sens.*, Vol. 30, 950–959, 1992.

19. Rodriguez, E. and J. M. Martin, "Theory and design of interferometic synthetic aperture radars," *IEE Proceeding — F Radar and Signal Processing*, Vol. 139, 147–159, 1992.
20. Li, F. K. and R. M. Goldstein, "Studies of multi-baseline spaceborne interderometric synthetic aperture radars," *IEEE Trans. Geosci. Remote Sens.*, Vol. 28, 88–97, 1990.
21. Gatelli, F., A. M. Guarnieri, F. Parizzi, P. Pasquali, C. Parti, and F. Rocca, "The wavenumber shift in SAR interferometry," *IEEE Trans. Geosci. Remote Sens.*, Vol. 32, 855–865, 1994.
22. Massonnet, D., "Capabilities and limitations of the interferometric cartwheel," *IEEE Trans. Geosci. Remote Sens.*, Vol. 39, 506–520, 2001.
23. Krieger, G., H. Fiedler, J. Mittermayer, K. Papathanassiou, and A. Moreira, "Analysis of multistatic configurations for spaceborne SAR interferometry," *IEE Proc. — Radar Sonar Navig.*, Vol. 150, 87–96, 2003.
24. Martone, M., B. Brautigam, and G. Krieger, "Decorrelation effects in bistatic TanDEM-X data," *Proceedings of IEEE Geoscience and Remote Sensing Symposium*, 5558–5561, Munich, Germany, 2012.
25. Brautigam, B., M. Martone, and P. Rizzoli, "Interferometric performance of TanDEM-X global DEM acquisitions," *Proceedings of 9th European Conference on Synthetic Aperture Radar*, 82–92, Nuremberg, Germany, 2012.
26. Cherniakov, M., *Bistatic Radar: Principles and Practice*, John Wiley & Sons, Chichester, England, UK, 2007.
27. Wang, T., Z. Bao, Z. Zhang, and J. Ding, "Improving coherence ofcomplex image pairs obtained by along-track bistatic SARs using range-azimuth prefiltering," *IEEE Trans. Geosci. Remote Sens.*, Vol. 46, 3–13, 2008.
28. Li, F. K. and W. T. K. Johnson, "Ambiguities in spaceborne synthetic aperture radar systems," *IEEE Trans. Aerosp. Electron. Syst.*, Vol. 19, 389–397, 1983.
29. Mcleod, I. H., I. G. Cumming, and M. S. Seymour, "ENVISAT ASAR data reduction: Impact on SAR interferometry," *IEEE Trans. Geosci. Remote Sens.*, Vol. 36, 589–602, 1998.
30. Li, H., R. Wu, and P. Han, "A robust estimation method to coregistration error for InSAR interferomrtric phase," *Proceedings of IEEE Radar Conference*, 283–286, Washing DC, USA, 2010.
31. Zhang, Y., D. Liang, and Z. Dong, "Analysis of time and frequency synchronization errors in spaceborne parasitic InSAR system,"

Proceedings of IEEE Geoscience Remote Sensing Symposium, 3047–3050, Denver, USA, 2006.

32. Weib, M., "Synchronisation of bistatic radar systems," *Proceedings of IEEE Geoscience and Remote Sensing Symposium*, 1750–1753, Anchorage, USA, 2004.
33. Lee, J. S., K. W. Hoppel, and S. A. Mango, "Intensity and phase statistics of multilook polarimetric and interferometric SAR imagery," *IEEE Trans. Geosci. Remote Sens.*, Vol. 32, 1017–1028, 1994.
34. Hillman, A., P. Rolland, M. Chabot, R. Periard, P. Ledantec, and N. Martens, "RADARSAT-2 mission operation status," *Proceedings of IEEE Geoscience Remote Sensing Symposium*, 3480–3483, Vancouver, Canada, 2011.